 CMES, vol.60, no.1, pp.41-71, 2010

Mesh Effects in Predictions of Progressive Damage in 3D Woven Composites

R. Valisetty[1,2], **A. Rajendran**[1,3] **and D. Grove**[2]

Abstract: A multi-scale model exhibiting progressive damage is considered for a 3D-woven composite. It is based on the evolution of some fundamental damage modes in a representative volume element (RVE) of a composite's woven architecture. The overall response of a woven composite due to a variety of damage modes is computationally obtained through a transformation field analysis (TFA) that is capable of quantifying the effects of spatial distribution of micro stresses and strains on strength. Since the model is computationally intensive, its numerical requirements are to be understood before it can successfully be used in design studies or in conjunction with Lagrangian explicit codes. This paper examines the effect of the local micro-mesh size on the progression of certain damage modes in 3D-woven composites and the predicted overall response.

Keywords: Fabrics/textiles, Stress concentrations, Impact behavior, Damage Mechanics

1 Introduction

Light weight armor material systems used in soldier and vehicle protection structures often involve synthetically engineered composite materials. The material design process requires the selection of configurations of material constituents and geometrical placements for optimal energy and momentum absorption. This process can be experimentally demanding, because the selected configuration is required to perform under transient impacts in which the material constituents deform and fracture in a controlled manner; the local damage modes spread in an orderly manner providing overall protection for the entire impact duration. Other than vast experimental data sets, procedures are not currently available to explain why certain combinations of materials and geometry are better at providing optimal energy

[1] Corresponding Author, raj@olemiss.edu, 662 915 5770 (off), 662 915 1640 (Fax)
[2] Comput. and Inform. Sciences Directorate, Army Research laboratory, APG, MD 21005
[3] Dept. of Mechanical Engineering, University of Mississippi, University, MS 38677

and momentum absorption, or how protection is achieved through local material damage and overall structural resistance.

Since impact response includes shock propagation, large deformation and brittle/plastic behaviors, theories used for selecting armor lay-ups must account for these behaviors. Such theories are available for homogeneous materials only. Procedures available to extend them to composites suffer from the simplicity of material aggregation, i.e. the effects of individual material micro-phases and micro-damage average out.

Accounting for such effects with continuously varying finite element meshes, i.e. a fine mesh at the micro-structural level that somehow transitions into a coarser one at the overall structure level, is not feasible owing to the difficulties of computer storage, numerical instabilities, etc. These difficulties can be overcome through multi-scale analyses using separate meshes to describe local material micro-structures and the global macro-structures. One such theory reported by Bahei-El-Din, Rajendran and Zikry (2004) used the transformation field analysis (TFA) of a representative volume element (RVE) of a 3D woven composite. It models up to nineteen different modes of damage which cover sliding and splitting of the fiber bundles in the warp, weft and z-direction and of material interfaces, as well as matrix damage modes in the woven composite.

Most computational approaches often focus on the overall impact response but not on how the micro-damage is affected by the built-up nature of the armor configuration. The link between the local damage modes and the overall response is described by the TFA in terms of stress concentration factors and influence functions, which reflect the geometry and properties of the constituents. In this way, the local geometry is represented in the model with substantial detail so that the local stress fields and the overall response are accurately computed in the presence of ongoing micro-damage progression.

While multi-scale theories were used before [Bogdanovich and Pastore (1996); Caiazzo, and Costanzo (2001); Oskay and Fish (2007); Ghosh, Lee, and Moorthy (1995)], the emphasis in those theories was on the global response, i.e. very fine meshes in the global domain and coarse ones in the local micro domain. Even when large local meshes are used, allowing the elements to totally fracture and form debris clouds doesn't yield clues as to the underlying damage mechanisms. Rather than modeling the material fragmentation, the RVE-TFA studies the effect of progression of certain apriorily selected damage modes on the local stresses and vice versa. This is achieved by introducing auxiliary transformation stress fields at levels that keep the micro damage modes under controlled progression. Additionally, by refining the local meshes of the RVE's, the damage modes' initiation and progression and the loss of ultimate stress carrying ability precipitated by individ-

ual damage modes is identified. This leads to a better understanding of the overall nonlinear response of the composite from the perspective of the underlying damage mechanisms.

RVE-TFA method takes a mechanics based view of the developing damage modes, i.e. a damage mode once initiated may grow unhindered but it controls and modifies the surrounding stresses. The evolving stress field may further initiate damage elsewhere in the microstructure indicating a weak damage mode interaction. Strong damage mode interaction in the form of stress-free-surfaces' creation is not considered, although such interaction can be implemented in RVE-TFA with the aid of fracture and erosion models. Even then, damage progressing in one RVE can not physically jump into and across other RVE's which is a limitation of the underlying multi-scale assumption under which theories like RVE-TFA are linked to global finite element analyses to provide overall stresses at integration points. Within the scope of the present work, material fragmentation and cracks jumping across RVE's are assumed to belong to the realm of macro-scale while the damage initiation to the micro-scale. The MLPG (Meshless Local Petrov-Galerkin) based computational algorithms developed by Atluri (2004) may be more suitable to describe the highly nonlinear fragment and fracture processes at macroscales. The computationally intensive TFA based constitutive models could utilize the theories developed by Han, Rajendran, Atluri (2005) to further handle nonlinear problems with large deformation and rotation. Recently, Liu, Han, Rajendran, and Atluri (2006) successfully modeled nonlinear problems involving projectile penetration into targets using MLPG approaches. The simulation results from the MLPG code were compared with finite element method (FEM) based code results that exhibited significant mesh distortions.

Multi-scale approaches offer a convenient method for analyzing modern armor structures which are engineered from materials of different length scales. While treating each material of a distinct length scale as a homogeneous material, it is imperative to consider the material's own intrinsic length scale which controls the specific damage modes that the material might experience. As a material is hot formed and then cold worked, its microstructure undergoes changes such as strain-induced anisotropy, localized shear bands, and micro-damage evolution. Various non-local, gradient based anisotropic damage mechanics theories were described by Voyiadjis and Kattan (2009) for treating a material's anisotropic damage mechanics, and were applied for studying armor composites under a high velocity impact, Abu Al-Rub and Voyiadjis (2006). Thus, the focus in this paper is to develop an understanding of damage initiation modes in a composite microstructure using the RVE-TFA approach.

When the locally computed micro-stresses in an RVE are aggregated, the over-

all stresses emerge for continuing the global analysis but such overall stresses do not bring any insight into the global domain about the locally progressing damage modes. From the perspective of the global analysis, the RVE-TFA multi-scale analysis might appear to be quasi static. But this view stems from the traditional reliance of RVE-TFA theories on stress formulations. The main RVE-TFA equations are usually dealt within the stress domain. Composite micromechanics theories used in the present work to model the progression of the damage modes are also cast in terms of stresses. The transient nature of RVE-TFA, however, is apparent when one considers the fact that there is an iteration involved in absorbing a global time step during which time local micro-analyses strive to cater to the local wave propagation and wave induced damage. While some local analyses [Bogdanovich and Pastore (1996); Caiazzo, and Costanzo (2001)] sub-cycle a global time step (in response to Courant stability criteria and micro-element sizes), TFA progresses existing damage modes while adding new-ones as needed.

Under low to moderate impact velocities, only long wave propagation can be observed in the global scale. It is possible that wavelengths that are of the same length scale as the constituents will have strong interactions where impedance mismatch related dispersions will greatly alter the local stresses. However, recent VISAR diagnostic based plate impact experiments on a glass reinforced laminate clearly showed the absence of wave attenuation and dispersion that can be attributed to material and geometrical mismatches at the RVE level. The measured wave profiles by Tsai, Prakash, Rajendran and Dandekar (2007) for a range of glass composite thicknesses and impact velocities indicated very little geometric dispersions and attenuations observed at the global level of the composite. Experimental studies by Chou and deLuca (1993) have shown that the stress wave propagation phase can induce significant damage. This micro-damage can be captured by TFA/hydrocode based analyses. Most of the quasi-static, Hopkinson bar based experimental stress-strain data for glass composites indicate mostly elastic behaviors; however, the inelasticity due to damage indicate strong strain rate effects on the failure stresses. The TFA based global analysis can include these rate dependent failure behaviors, e.g. the recent extension of present work by Bahei-El-Din, Rajendran, Valisetty, and Namburu (2007). The present work is however limited to rate-independent damage modes in order to focus the study on the local RVE mesh sensitivity.

The earlier focus in the RVE-TFA work was on obtaining the local microscopic stresses and relating them to overall stress increments for conducting global-local modeling and on parallelizing the attendant computation, Valisetty, Namburu, Rajendran, and Bahei-El-Din (2004). The RVE-TFA damage model was implemented into the DYNA3D finite element code, and simulations of impact problems were performed to capture the material heterogeneity and spreading local damage. RVE-

TFA is but one approach to multi-scale formulation of composite micro-mechanics and micro-damage; the others include homogenization [Bogdanovich and Pastore (1996); Caiazzo, and Costanzo (2001)] micro-eigen-deformations [Oskay and Fish (2007)], Voronoi cell finite element method [Ghosh, Lee, and Moorthy (1995)]. Although an RVE mesh size affects the results and increases the computations, the mesh effect was not studied in detail in the past. In this context, the present work was undertaken to study the effect of the RVE mesh size on the computed overall stresses and on micro-damage progression for a 3-D woven composite. The micro-damage induced strength degradation is noted from the computed stress-strain response for the RVE and was ascribed to the prevalent damage modes.

2 RVE-TFA Equations for Local Stresses

Fig. 1 shows a typical RVE that can be used for modeling a 3-D woven composite. Overall dimensions of the RVE are not arbitrary. They are determined from actual micrographs of the woven system. While the number of sub-volumes in an RVE or its mesh size can be arbitrary, it is convenient to have each RVE sub-volume belonging to a distinct material or phase (fiber bundle, matrix, or interface).

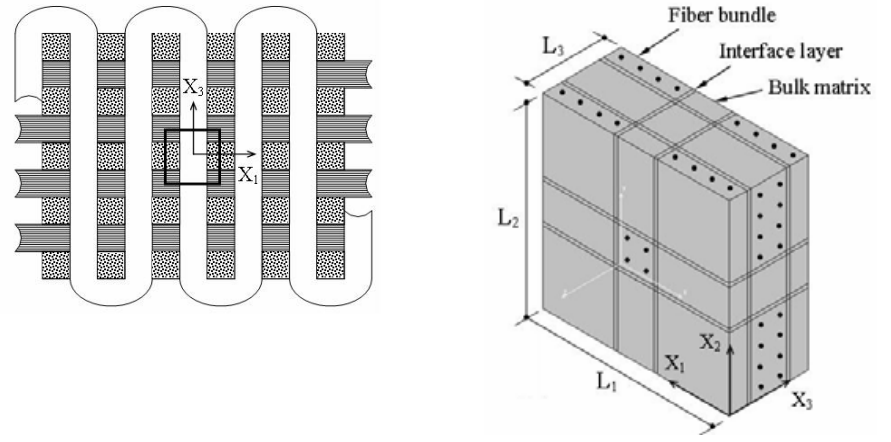

Figure 1: A Schematic of a 3D woven composite and material placement for a representative volume element

The RVE-TFA approach rests on the fact that an RVE can be used to model the point-wise and piecewise uniform variation of stress fields at integration points in a global Lagrangian analysis of a composite as sums of elastic stresses caused in the undamaged composite by the applied overall loads and self-equilibrating local

transformation stress fields. Each of the transformation stress fields is associated with an on-going damage mode within the RVE and its magnitude is determined to keep the local stresses at levels to meet the underlying damage criteria. The transformation stress fields thus found depend on the number of damage modes considered and how many of these become active. This in turn may depend on the refinement of the descritized local stress field. In between the time steps of the global Lagrangian analysis, damage initiation and progression is considered in the RVE's and the response is determined by the RVE-TFA analysis. Hence, the method in this context is essentially a two-level multi-scale analysis.

Original formulation of the TFA approach is due to Dvorak (1992), who later extended it to inelastic composites [Dvorak, Bahei-El-Din, and Wafa (1994)] and modeling interface damage [Dvorak and Zhang (2001)]. Bahei-El-Din and Botrous (2003) used the method to model fiber debonding in laminates, and Bahei-El-Din, Rajendran and Zikry (2004) extended the TFA analysis to the study of plate impact problems of 3-D woven composites by considering a full complement of damage modes. While Bahei-El-Din, Rajendran and Zikry (2004) presented the full set of the RVE-TFA equations, only those equations from this set related to the overall and transformation stresses are presented next to facilitate the discussion of the progression of the local damage modes and their role in correcting the local stresses. This is done using a notation of boldface lower case letters for representing the (6x1) stress vectors, and boldface upper case letters for representing the corresponding stiffness matrices as well as stress concentration factors.

$\bar{\sigma}$, the global stresses at an integration point where an RVE is called, are weighted volume sum of σ_r, the local sub-volume stresses:

$$\bar{\sigma} = \sum_{r=1}^{Q} c_r \sigma_r. \tag{1}$$

Q is the number of sub-volumes and c_r the sub-volume fractions. The local sub-volumes are assumed to undergo elastic deformation. Deviations from this mode of deformation, for accounting the effects of damage, are treated by adding transformation fields. A part of the local sub-volume stresses can be related to the global applied loads following the treatment of elastic composite aggregates by Hill (1963 and 1965), the rest to the transformation fields originating in all local sub-volumes within the RVE [Dvorak (1992)]. Superposition of these effects provides the total strains and stress in the sub-volumes:

$$\sigma_r = B_r \bar{\sigma} + \sum_{s=1}^{Q} F_{rs} \lambda_s, \quad r = 1, \ldots, Q \tag{2}$$

B_r are stress concentration factors, and F_{rs} are stress transformation influence factors and λ_r are transformation stresses, respectively.

The elements of B_r and F_{rs} depend upon the local geometry and properties and can be determined from an elastic analysis of the undamaged RVE. Columns of B_r represent local stresses caused by unit overall stresses applied to the RVE. For example, the k^{th} column, $k = 1,\ldots,6$, of the stress concentration factors, B_r, $r = 1,2,\ldots,Q$, is computed by giving a unit value to the k^{th} stress component and 0 to the rest of the stresses in the 6×1 overall stress vector, $\bar{\sigma}$. This is done by a finite element solver in which a linear local displacement field is assumed in sub-volumes of the RVE. Certain displacement conditions are applied to reflect the periodicity of the microstructure and to prevent rigid body motions [Dvorak and Teply (1985)]. A similar procedure is also used for computing F_{rs} by realizing that a k^{th} column, $k = 1,2,\ldots,6$, of F_{rs}, $r,s = 1,2,\ldots,Q$, is the stress in sub-volume V_r due to a unit stress, $\lambda_k = 1$ residing in sub-volume V_s. A total of $6Q$ RVE finite element solutions are required to completely evaluate the transformation factors. Once B_r and F_{rs} are available, then the task of determining λ_r remains; this will be described next.

3 Damage modes and progression

In the RVE-TFA formulation described so far, the problem is reduced to finding the local transformation stresses. When local constituents are elastic and when there is no damage, the local stresses caused by the applied loads are given entirely by the stress concentration factors, which essentially capture material heterogeneity. These elastic stresses begin to change when damage modes appear and start progressing. When local constituents become damaged, then the transformation stresses are used to offset the local stresses from their pre-damage values to levels dictated by the local damage criteria. This approach is amenable to handling specific damage modes. For example, in Dvorak and Zhang (2001), Bahei-El-Din and Botrous (2003) and Bahei-El-Din (1996), the interfacial stresses found at the onset of fiber debonding are computed by introducing transformation stresses. Other forms of damage can be treated similarly to satisfy the underlying damage criteria. Superposition of the elastic stresses and the transformation stresses provide the total stresses.

For an RVE with Q sub-volumes, V_ρ, $\rho = 1,2,...,Q$, the stresses in the undamaged state can be found in terms of the overall stress as $B_r\bar{\sigma}$ (Eq. $(2)_2$). Suppose now there is damage in some sub-volumes, V_ρ, $\rho = 1,2,...,Q^*$, $Q^* \leq Q$, of the RVE. The computed elastic stresses will then exceed the underlying strength values in those sub-volumes. To bring the computed elastic stresses to conform to the requirements of the damage criteria of the locally progressing damage modes, transformation stresses are introduced and evaluated. The transformation stresses

are evaluated by recasting Eq. (2). This is done by recognizing that on the right hand side of Eq. (2), the first parts, $B_r\,\bar{\sigma}$ are the elastic stresses and the second parts, $\sum_{s=1}^{Q} F_{rs}\lambda_s$ are the transformation stresses, and together these two parts equal to the current local stresses on the left hand side of Eq. (2). Hence, the transformation stresses are evaluated by setting the current stresses on the left hand side to values that do not violate the damage criteria.

Next, to present the equations and later damage modes and their growth criteria, local stresses are considered in local coordinate systems with appropriate co-ordinate transformation matrices, R_ρ. The local coordinate systems are not unique; they change depending on the sub-volume phase orientations and specific damage criteria. For example, a tensile damage in a fiber bundle is best described with the 3^{rd} axis of the local co-ordinate system aligned along the fiber bundle axis. Referring to such local coordinate systems and using stress ratios, $\varphi_k^{(\rho)}$, which are current stresses divided by their elastic undamaged values, the equations for computing transformation stress are given by Bahei-El-Din, Rajendran and Zikry (2004):

$$\sum_{\eta=1}^{Q^*} F_{\rho\eta}\,diag(\alpha_k)\lambda_\eta = -(I - R_\rho^{-1}\,diag(\varphi_k^{(\rho)})R_\rho)\,B_\rho\,\bar{\sigma}\,, \quad \rho = 1,2,,Q^*, \tag{3}$$

$$\alpha_k = \begin{cases} 1 & if\ 0<\phi<1 \\ 0 & if\ \phi = 1 \end{cases}, \tag{4}$$

where $diag(\mathbf{x})$ is a (6×6) matrix. The stress ratios, $\varphi_k^{(\rho)}, k = 1,2,...,6,\ \rho = 1,2,...,Q^*, Q^* \le Q$, imply pre- and post-damage loading as follows: $\varphi_k^{(\rho)} = 1$ for a stress component that has not violated the onset of damage, $\varphi_k^{(\rho)} = 0$ indicates complete unloading, and $0 \le \varphi_k^{(\rho)} \le 1$ indicates progressing damage with partial property decay.

If $\varphi_k^{(\rho)} < 1$ for all $k = 1,2,\ldots,6$ and for all Q^* sub-volumes, then there are $6Q^*$ equations in Eq. (3) for evaluating the transformation stresses. If some of the local stress components are unaffected by the underlying damage criteria, the corresponding stress ratios would equal unity. In such cases, $\alpha_k = 0$, and the corresponding transformation stresses will not be needed and enough equations will drop out from (3). The equations available after this consideration are solved for the remaining transformation stresses.

3.1 Damage modes

Although the RVE-TFA analysis is completed by updating the local stresses with contributions from the transformation stresses, its description here is not complete

without mentioning the specific damage modes that are considered in this work which uses the RVE-TFA code of Bahei-El-Din, Rajendran and Zikry (2004). It considers damages of fiber bundles, interface layers, and matrix. Four damage modes are considered in the fiber bundles as follows: longitudinal fiber rupture, transverse and longitudinal inter-bundle fiber sliding, and transverse inter-bundle fiber splitting. Shear sliding and peeling damage modes are considered in the interface layers. The bulk matrix damage is assumed to be terminal.

While interaction can be expected between the progressing damage modes active within an RVE, some damage modes can progress without interaction within a material. For example, sliding damage modes on transverse and longitudinal planes within a fiber bundle are interactive, while sliding and splitting of the interfaces are independent. The stress ratios, φ_k, which are introduced to keep track of the damage progression, become unique and independent when the corresponding damage modes do not interact; while the stress ratios involved in the interacting damage modes are not unique. For such interacting modes, the stress ratio of the weakest damage modes is selected.

3.2 Damage Progression

The damage progression is implemented with the aid of numerical loading and relationships between resolved scalar stress and strain quantities, (s, e). The definitions of s and e change with the nature of damage modes. The s-e relationships can be computed with the knowledge of the local stresses and the evolving damage modes. The linear elastic limit is defined by the ultimate strength, s_{ult}, and the corresponding strain, e_{el}. The softening branch can take a linear or a nonlinear form defined symbolically as $s = g(e - e_{el})$, where $e_{el} \leq e \leq e_{ult}$, and e_{ult} is the ultimate strain. Unloading/reloading followed a linear path between the origin and the (s, e) curve. For a given total strain $e^{(i)}$, at the i^{th} numerical loading step of the applied load, the elastic stress is computed as $s^{(i)} = (s_{ult}/e_{el})e^{(i)}$, which may or may not fall on the s-e curve. The correct stress magnitude, and hence the current stress ratio, $\varphi^{(i)}$, is determined from the response expected by the s-e curve and the values of $s^{(i)}$, $e^{(i)}$, and $\varphi^{(i-1)}$, the stress ratio at the previous step, as follows:

$$\begin{aligned} &undamaged\,state: \quad \phi^{(i)} = 1, \quad if\ \phi^{(i-1)} = 1, \quad 0 \leq e^{(i)} < e_{el} \\ &damage\,reversal: \quad \phi^{(i)} = \phi^{(i-1)}, \quad if\ \phi^{(i-1)} < 1, \quad 0 \leq e^{(i)} < e_{el} \end{aligned}, \tag{5}$$

$$continued\,damage:\ \phi^{(i)} = \frac{g(e^{(i)} - e_{el})}{s^{(i)}},\ if\ \frac{g(e^{(i)} - e_{el})}{s^{(i)}} < \phi^{(i-1)},$$
$$e_{el} \le e^{(i)} < e_{ult}. \quad (6)$$

$$damage\ reversal:\ \ \phi^{(i)} = \phi^{(i-1)}, if\ \frac{g(e^{(i)} - e_{el})}{s^{(i)}} > \phi^{(i-1)}, e_{el} \le e^{(i)} < e_{ult}$$

The first condition in Eq. (5) represents the response of an undamaged material. The first condition in Eq. (6) describes continued loading of a previously damaged state. The second conditions represent linear unloading/reloading from a damaged state. Hence, damage is tracked by recording the loading history of the incremental values of the stress ratio $\varphi_k^{(i)}$.

The stress and strain pair at the current loading step ($s^{(i)}$, $e^{(i)}$), has different interpretations depending on the type of the RVE constituent and the associated damage mode. In what follows, these quantities are related to the local stress and strain averages. It is assumed that the total overall stress $\bar{\sigma}^{(i)}$ at the current loading step is known, either directly by following a defined, stress-controlled loading path, or as the stress $\bar{L}\bar{\varepsilon}^{(i)}$ caused in an undamaged RVE by a strain-controlled loading.

$$\hat{\sigma}_r^{(i)} = \mathbf{R}_r \mathbf{B}_r \bar{\sigma}^{(i)}, \quad \hat{\varepsilon}_r^{(i)} = \hat{\mathbf{M}}_r \hat{\sigma}_r^{(i)}, \quad r = 1, 2, \ldots, Q. \quad (7)$$

Matrix $\mathbf{R}_r$ relates the stresses described in the local and the overall coordinate systems, and $\hat{\mathbf{M}}_r$ is the elastic compliance described in the local axes. Expressions for $s^{(i)}$ in terms of the resolved stress $\hat{\sigma}$ and material properties e_{el}, e_{ult}, s_{ult} for the present damage modes are provided in Tab. 1. The bulk matrix damage is treated as irrecoverable.

4 Results

In this section, numerical results are presented to examine the RVE mesh size effect on the RVE-TFA predictions. For this purpose, a 3D woven composite made of S2-glass/epoxy system is used. The composite was evaluated to have the micro-geometry shown in Fig. 2. As seen in the micrographs of Fig. 2a, the fiber bundle in the warp and weft directions has a rectangular cross-section with aspect ratio of about 4.0, while the z-fiber bundle has a square cross-section. The dimensions of the RVE parallel to the overall in-plane axes were taken as 12mm and 12mm and in the z-direction as 2.2mm.

For demonstrating the RVE mesh size effect on modeling the local damage modes, the type of global analysis— quasi-static or transient— is not an issue. Wave attenuation observed in global scale can be attributed to micro-damage which in turn

Table 1: Damage criteria in terms of resolved stresses

Damage modes	Damage condition	Strain at damage initiation e_{el}	Strain at ultimate failure e_{ult}
Fiber bundle rupture	$s = \hat{\sigma}_{11}$, $e = \hat{\varepsilon}_{11}$, where, E_L = longitudinal Young's modulus	$\varepsilon = \sigma^L_{ult} / E_L$	σ^L_{ult} / E_L
Transverse inter-bundle fiber sliding	$s = \lvert\tau^{max}_{ns}\rvert + \mu_T \langle\sigma_n\rangle$ and $e = \gamma^{max}_{ns} = \tau^{max}_{ns} / G_T$, where, μ_T = coef. of friction, G_T =trans.shear modulus $\tau^{max}_{ns} = \pm\frac{1}{2}\sqrt{(\hat{\sigma}_{22} - \hat{\sigma}_{33})^2 + 4\hat{\sigma}^2_{23}}$, $\sigma_n = \frac{\hat{\sigma}_{22} + \hat{\sigma}_{33}}{2}$ $\beta = \frac{1}{2}\tan^{-1}\left\lvert\frac{\hat{\sigma}_{33} - \hat{\sigma}_{22}}{2\hat{\sigma}_{23}}\right\rvert$,	$\gamma^T_{el} = \frac{\tau^T_{ult}}{G_T}$	γ^T_{ult}
Longitudinal inter-fiber sliding	$s = \lvert\tau^{max}_{ns}\rvert + \mu_L \langle\sigma_n\rangle$ and $e = \gamma^{max}_{ns} = \tau^{max}_{ns} / G_L$ where, $\tau^{ns}_{max} = \pm\sqrt{\hat{\sigma}^2_{12} + \hat{\sigma}^2_{13}}$, G_L =long. shear modulus $\sigma_n = \frac{\hat{\sigma}_{22}\hat{\sigma}^2_{12} + \hat{\sigma}_{33}\hat{\sigma}^2_{13} + 2\hat{\sigma}_{23}\hat{\sigma}_{31}\hat{\sigma}_{12}}{\hat{\sigma}^2_{12} + \hat{\sigma}^2_{13}}$, $\beta = \tan^{-1}\left\lvert\frac{\hat{\sigma}_{31}}{\hat{\sigma}_{32}}\right\rvert$	$\gamma^L_{el} = \frac{\tau^L_{ult}}{G_L}$	γ^L_{ult}
Transverse inter-bundle fiber splitting	$s = \sigma^{max}_n$ and $e = \varepsilon = \frac{\sigma^{max}_n}{E_T}$ where, $\sigma^{max}_n = \frac{1}{2}(\hat{\sigma}_{22} + \hat{\sigma}_{33}) + \frac{1}{2}\sqrt{(\hat{\sigma}_{22} - \hat{\sigma}_{33})^2 + 4\hat{\sigma}^2_{23}}$ $\beta = \frac{1}{2}\tan^{-1}\left[\frac{2\hat{\sigma}_{23}}{\hat{\sigma}_{33} - \hat{\sigma}_{22}}\right]$, E_T =transverse modulus	$\varepsilon^T_{el} = \frac{\sigma_{ult}}{E_T}$	$\varepsilon^T{}_{ult}$
Interface shear sliding	$s = \lvert\tau\rvert + \mu\langle\sigma_n\rangle$ and $e = \gamma = \frac{s}{G_m}$ where, $\tau = \pm\sqrt{\hat{\sigma}^2_{32} + \hat{\sigma}^2_{13}}$, $\sigma_n = \hat{\sigma}_{33}$	$\gamma_{el} = \frac{\tau_{ult}}{G_m}$	γ_{ult}
Interface peeling	$s = \hat{\sigma}_{33} \geq 0$ and $e = \varepsilon = \frac{s}{E_m}$	$\varepsilon_{el} = \frac{\sigma_{ult}}{E_m}$	ε_{ult}
Bulk matrix failure	Failure envelope: $f = \frac{\hat{\sigma}^2_{eff}}{\hat{\sigma}^2_{ult}} + 3\frac{\hat{\tau}^2_{eff}}{\hat{\tau}^2_{ult}} - 1 = 0$, where, $\hat{\sigma}^2_{eff} = \hat{\sigma}^2_{11} + \hat{\sigma}^2_{11} + \hat{\sigma}^2_{11} - \hat{\sigma}_{11}\hat{\sigma}_{22} - \hat{\sigma}_{33}\hat{\sigma}_{22} - \hat{\sigma}_{11}\hat{\sigma}_{33}$, $\hat{\tau}^2_{eff} = \hat{\sigma}^2_{12} + \hat{\sigma}^2_{23} + \hat{\sigma}^2_{31}$, and a stress state outside failure envelope is not possible which means that $\varphi^{(t)} = 1$, if $f < 0$ and $\varphi^{(t-1)} = 1$, $\varphi^{(t)} = 0$, if $f < 0$ and $\varphi^{(t-1)} = 0$, and an undamaged state can not be recovered. $\varphi^{(t)} = 0$, if $f \geq 0$		

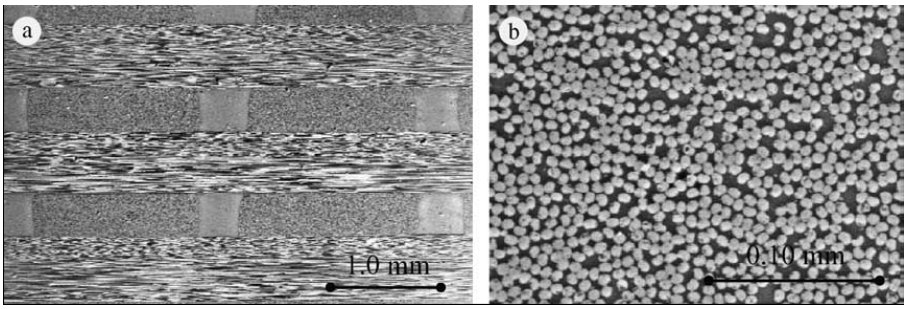

Figure 2: Micrographs of a 3D-woven, glass/epoxy composite [Qiu, Xu, Wang, and Zikry (2001)]: (a) cross-section through longitudinal direction of the warp fiber bundle and (b) cross-section through the weft fiber bundle

can be affected by strain rate. Since the effect of strain rate in increasing the failure stress is easily included in RVE-TFA formulations [Bahei-El-Din, Rajendran, Valisetty, and Namburu (2007)], this effect is not considered in the present study so as to focus the present study only on the mesh effect. As mentioned before, for low to moderate impact velocities, the globally observed stress wave propagation does not show much dispersion that can be attributed to any specific geometry and material mismatch in the RVE. Since the global and local analyses occur at different length scales, the mesh requirements in one scale domain can not affect the mesh requirements in the other length scale domain. Since local solutions are iterated in response to locally spreading damage with sufficiently fine RVE meshes, the issues in global scale such as the shape of an impactor can not affect the element size selection for the RVE mesh. Naturally, the global elements should be sized to accommodate global structural features. Although relative, not absolute, dimensions control an RVE's results, there can be size effect when the RVE-TFA analysis is applied to (a few lamina) thin global laminates.

The fiber bundles in the warp, weft and z-directions were treated as fibrous composites and the fiber volume fraction was determined from the densities of the woven composite samples and the dry fabric. This led to an overall fiber volume fraction of 0.42, and a volume fraction for the yarn in the bundle of 0.57. The glass yarn was assumed to be transversely isotropic. Only the longitudinal elastic modulus can be found in published data, while the remaining moduli and strength data were assumed. Using the elastic properties of the isotropic epoxy matrix and the Mori–Tanaka material model, elastic moduli of the glass/epoxy fibrous composite were estimated. The properties shown in Tab. 2 were used for the RVE constituents.

For the composite, several RVE idealizations can be constructed beginning with the

Table 2: Properties of the 3-D woven, glass/epoxy composite and its constituents

	Fiber bundle	Resin
E_L	59.7	2.9
E_T	11.7	2.9
ν_{LT}	0.248	0.3
ν_{TT}	0.371	0.3
G_{LT}	5	1.12
G_{TT}	4.68	1.12
$\sigma_{max\text{-}L}$	3.36	0.06
σ_{max-T}	0.08	0.06
ε_T	0.0068	0.021
ε_{max-T}	0.0068	0.021
τ_{max-L}	0.057	0.035
γ_L	0.0114	0.0313
γ_{max-L}	0.0114	0.0313
τ_{max-T}	0.048	0.035
γ_T	0.0112	0.0313
γ_{max-T}	0.0112	0.0313

Table 3: Mesh size vs. size of the set of the Transformation Influence Factors

Mesh ID	No. of Elements	Size of the set of the Transformation Influence Factors
1	150	810000
2	294	3111696
3	490	8643600
4	882	28005264
5	1458	76527504
6	2106	159668496
7	2366	201526416

simple one shown in Fig. 1. In Fig. 1b, an approximate material placement of the fiber bundles in the warp, weft and z directions, and the resin and interfacial layers is shown. For the numerical study, this idealization is selected. To begin the study, several RVE meshes were considered as shown in Fig. 3. Once again several possibilities existed for increasing the sub-volumes, but the indicated preponderance of sub-volumes in the z-direction was in view of the intended application of the RVE-TFA in composite armor impact design studies. Other than increasing number of sub-volumes, these meshes do not share any other geometric characteristics,

e.g. mesh symmetry or density in x, y, z directions. Therefore the results obtained with the selected meshes can not be interpreted as indicating mesh convergence in a general sense.

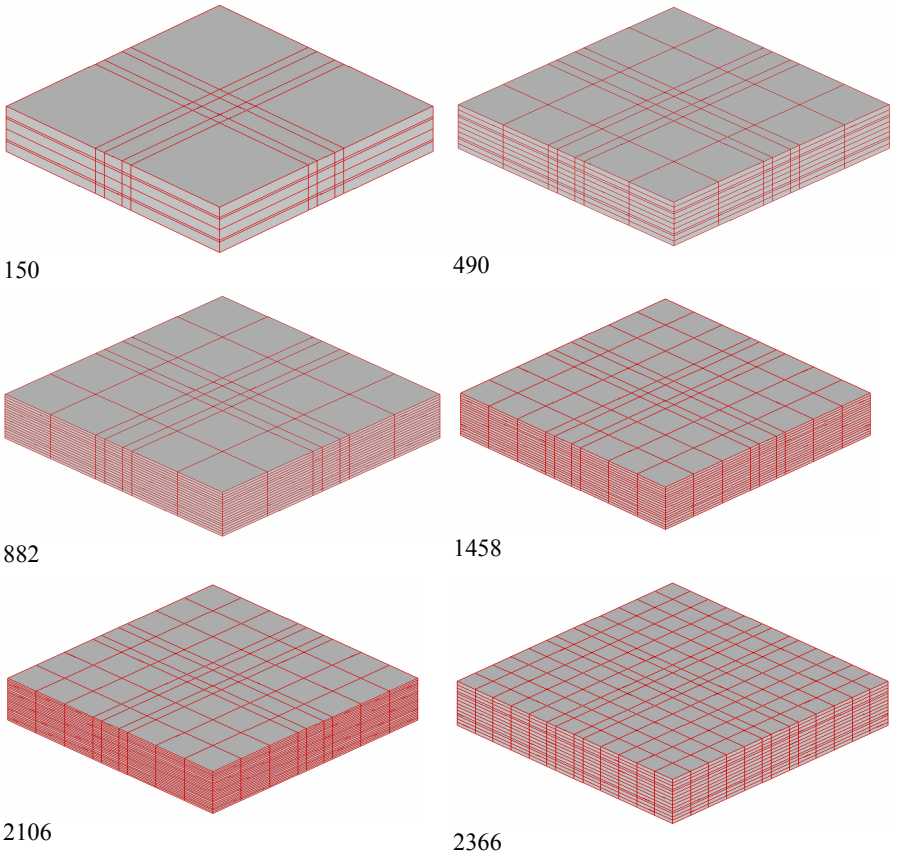

Figure 3: Different finite element meshes considered for the RVE microstructure

In the TFA approach, the effect of local damage on the stress field in the RVE is determined with the aid of stress transformation factors, F_{rs}(Eq. $(3)_2$). The larger the number of the sub-volumes in the RVE, the larger is the size of F_{rs}, which is computed apriori using a finite element analysis of an undamaged, elastic RVE. The storage required for the F_{rs} factors is given in Tab. (3) for the meshes indicated in Fig. 3. In reality there could be a weak interaction between some sub-volumes of the RVE which are far from each other. With a small tolerance factor, F_{rs} factors contributing to such weak interaction were removed. Tab. 3 shows the motivation for the present work. Either for using the RVE-TFA in a stand-alone manner for

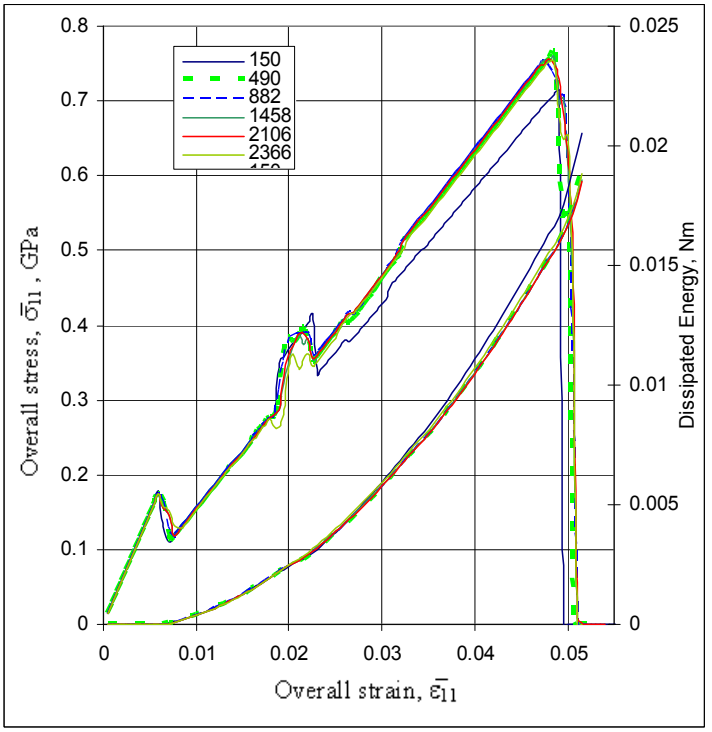

Figure 4: Effect of micromesh size on computed overall $\bar{\sigma}_{11}$ vs. $\bar{\varepsilon}_{11}$ response

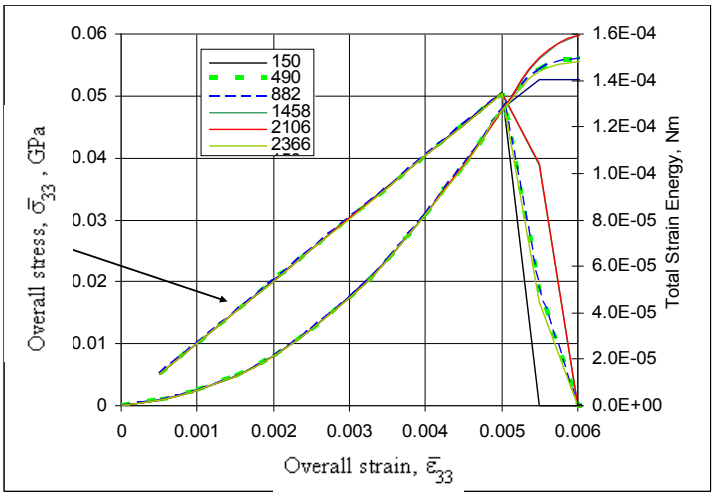

Figure 5: Effect of micromesh size on computed overall $\bar{\sigma}_{33}$ vs. $\bar{\varepsilon}_{33}$ response

evaluating armor composite designs or as a subroutine for evaluating the overall macro-element stresses in a multi-scale analysis, the success depends on the turn-around time of the RVE-TFA analysis. An important determinant of this time is the number of the F_{rs} factors, which depends of the RVE mesh size. In this context and in view of the F_{rs} sizes in Tab. (3), the present mesh sensitivity study was conducted.

In this study, overall stress-strain curves were computed for the 3-D woven composite by considering each of the four following loading cases separately: (1) $\bar{\sigma}_{11}$ vs. $\bar{\varepsilon}_{11}$, (2) $\bar{\sigma}_{33}$ vs. $\bar{\varepsilon}_{33}$, (3) $\bar{\tau}_{12}$ vs. $\bar{\gamma}_{12}$, and (4) $\bar{\tau}_{23}$ vs. $\bar{\$}\gamma_{23}$. The $\bar{\sigma}_{22}$ vs. $\bar{\varepsilon}_{22}$ and $\bar{\tau}_{13}$ vs. $\bar{\gamma}_{13}$ responses match the $\bar{\sigma}_{11}$ vs. $\bar{\$}\varepsilon_{11}$ and $\bar{\tau}_{23}$ vs. $\bar{\$}\gamma_{23}$ responses, respectively, because of the RVE symmetry. In each loading case, the indicated overall strain was applied to the RVE while the other overall strains were held to zero. The corresponding overall stress was recorded from the TFA analysis. The analyses also gave local stresses and active damage modes as the overall strains were incremented. These results are summarized under the categories of overall stress vs. strain curves, local stress distributions, and damage progression.

4.1 Overall stress vs. strain curves

The overall stress-strain curves are presented in Figs. 4-7 for the four overall strain-controlled loading cases and the meshes shown in Fig. 3. Also shown is the strain energy density accumulated as a function of the applied strain. It is seen that details of the predicted stress-strain response, including softening due to damage which has been observed experimentally [Shah Khan and Simpson (2000), Kim and Sham (2000)] are captured by all subdivisions of the RVE. Since total damage is attained, the end point of each strain energy curve indicates the magnitude of energy dissipated per unit volume due to damage during the respective loading regimes. This is compared for the various subdivisions of the RVE in Fig. 8. A similar comparison is shown in Figs. 9 and 10 for the peak stress and ultimate strain found from the stress-strain curves of Figs. 4-7.

The results indicate that the response predicted by the very fine meshes of the RVE can be reproduced with a small margin of error by a more coarse mesh. While increasing the mesh size from 150 sub-volumes to 490 leads to a somewhat significant change in some computed results, further mesh refinement appears to produce rather small changes. In particular, the RVE with 490 sub-volumes produces results comparable to those provided by much finer meshes. For larger meshes, the discrepancies are small and are outweighed by the substantial savings realized in the computation cost.

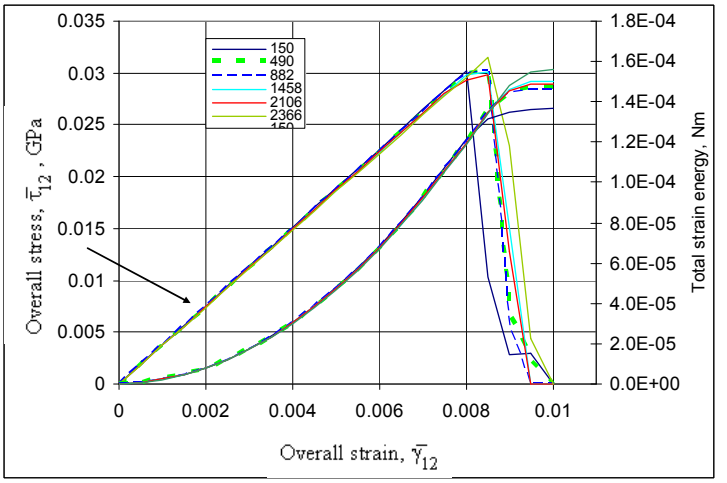

Figure 6: Effect of micromesh size on computed overall $\bar{\tau}_{12}$ vs.$\bar{\tau}_{12}$ response

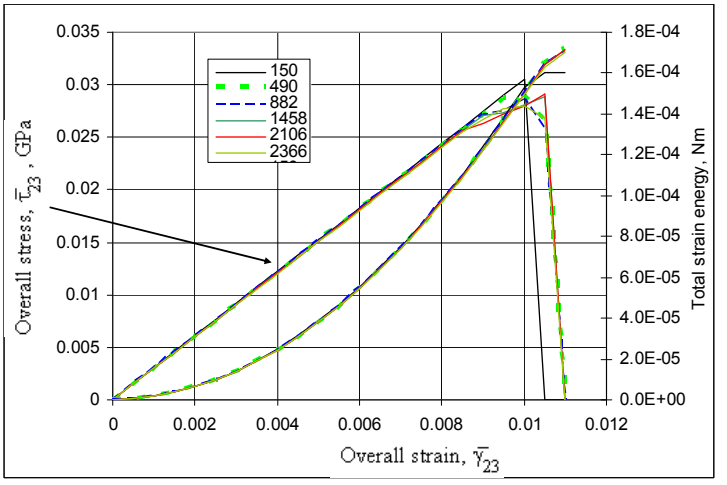

Figure 7: Effect of micromesh size on computed overall $\bar{\tau}_{23}$ vs. $\bar{\tau}_{23}$ response

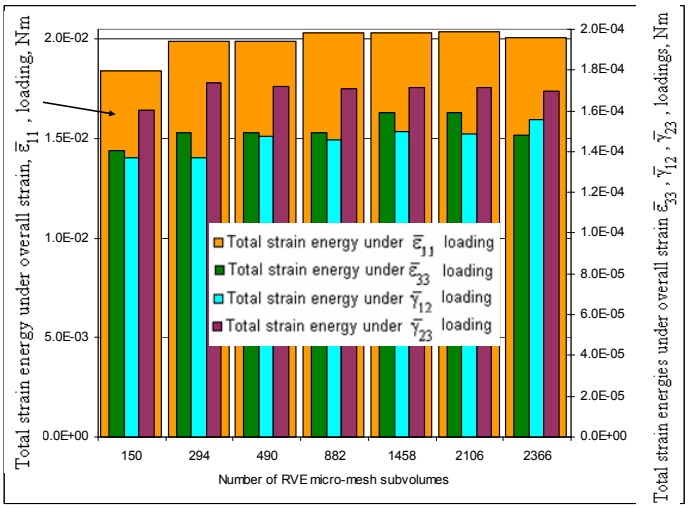

Figure 8: Effect of micromesh size on total strain energy at total damage

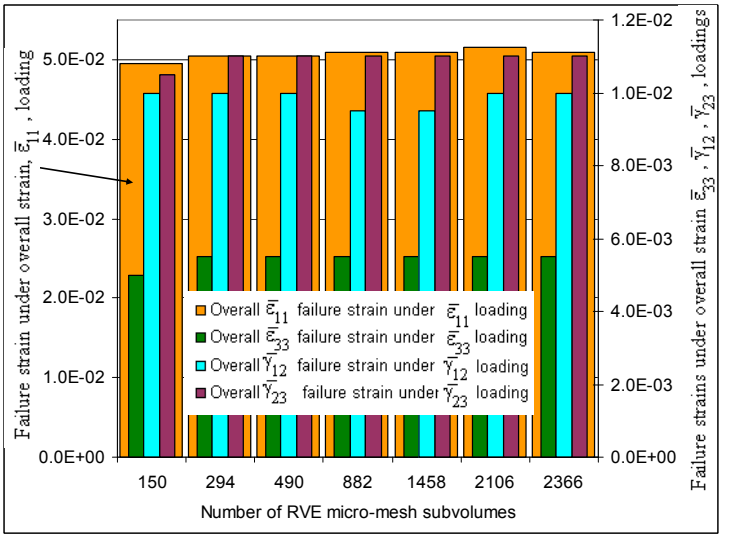

Figure 9: Effect of micromesh size on overall applied strains at total damage

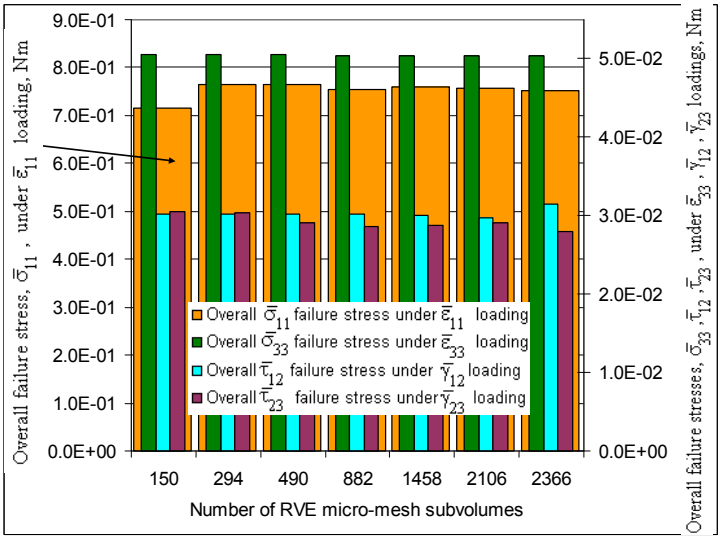

Figure 10: Effect of micromesh size on predicted maximum overall stresses

4.2 Local stress distributions

The results for the local stress distributions in the RVE are presented in Figs. 11-14. To begin with, the effect of micromesh size on the computed local $\bar{\sigma}_{11}$ distribution is shown in Fig. 11 on the lower half of the RVE at an applied overall strain, $\bar{\varepsilon}_{11}$, of 1%. This figure clearly indicates that there is agreement in the stress distribution predictions with respect to the increasing mesh sizes. Among the mesh sizes considered, the 490 mesh size is smallest mesh size that is successful at being able to predict both the trend as well as the extreme stress values. Similar trend was also found for other overall strain values.

In Fig. 12, the out-of-plane normal stress distribution results are compared for all the meshes involved in this study after applying an overall through-thickness strain, $\bar{\varepsilon}_{33}$, of 0.55%. Since the numerical range is small for this strain, stress distributions at other strain values are not considered, and even the strain value used for these figures is very close to its failure limit. In Figs. 13 and 14, the longitudinal shear stress and the transverse shear stress distributions are similarly compared. For all the three stresses, the distributions are characterized by the acuteness of the stress concentrations which happens because there is not much interface layer material in the RVE to transfer these stresses across the matrix and fiber bundles, see, Fig. 12, for the stress concentration in the z fiber bundle, and, Fig. 13, for the stress concentration in the thin interface layers. In spite of this, similar conclusions are

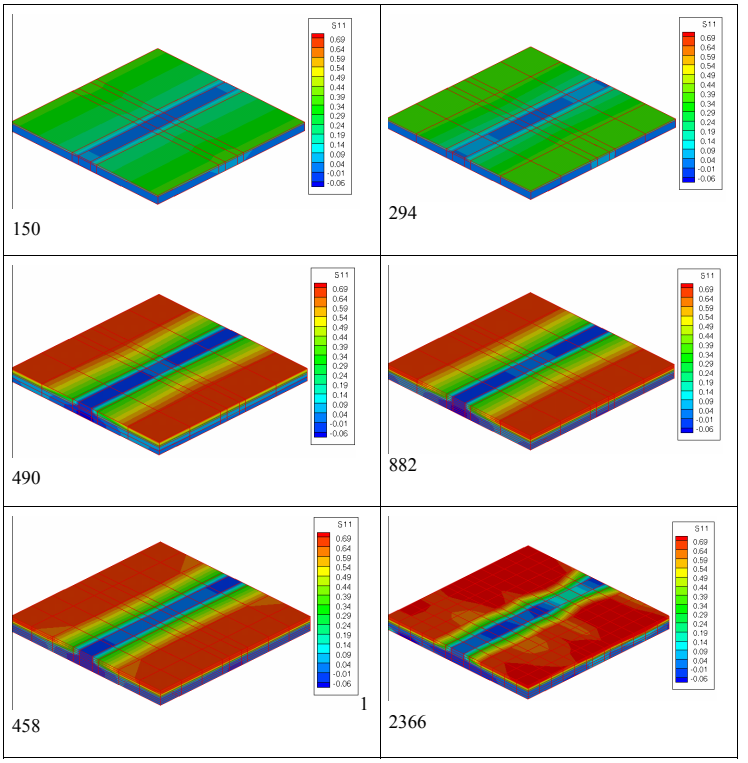

Figure 11: Effect of micromesh size on the computed local $\bar{\sigma}_{11}$ distribution, shown on the lower half of the RVE, applied overall strain $\bar{\varepsilon}_{11}$= 1%

once again drawn for the mesh size effect and the 490 mesh size is deemed the smallest of the mesh sizes that begins to predict the stresses.

4.3 Damage progression

In Figs. 4-7, the effect of damage can be seen on the overall stress vs. strain curves but not the specifics of the causative damage modes. Several damage modes were discussed in Section 3 and was said that the progression of damage modes was not considered explicitly by allowing for the fragmentation of sub-volumes. The progression was considered indirectly by letting the progressing damage modes control the local stresses in the RVE sub-volumes. In this sense, if a particular damage mode is observed to be controlling local stresses in some RVE sub-volumes, then the total number of all such sub-volumes is tracked as an indirect measure of the progression for that particular damage mode. In a similar manner, the progres-

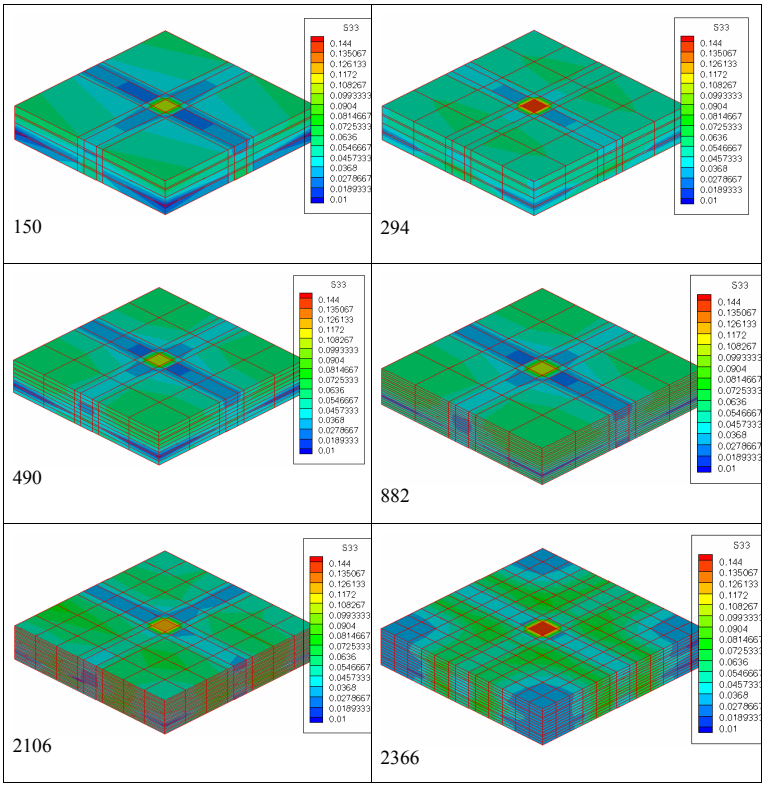

Figure 12: Effect of micromesh size on the computed local $\bar{\sigma}_{33}$ distribution, applied overall strain $\bar{\varepsilon}_{33}$= 0.55%

sion of all the damage modes is monitored by keeping track of the number of all damaged sub-volumes.

In Figs. 15-17, the overall stress vs. overall strain plots are superimposed by the plots of individual counts of the damaged sub-volume accumulations for each of the active damage modes. These results were obtained under strain-controlled loading in which one (overall) strain component was increased while the other five (overall) strain components were held at zero. For in-plane tensile loading, Fig. 15, several damage modes appear but the dominant ones in the order of their rapid growth may be listed as: fiber splitting normal to the load direction, fiber sliding due to transverse shear decay, fiber sliding due to transverse tension, matrix peeling, etc. The important fiber failure due to axial tension doesn't become significant until the (overall) strain reaches 4.75% after which the overall stress drops precipitously.

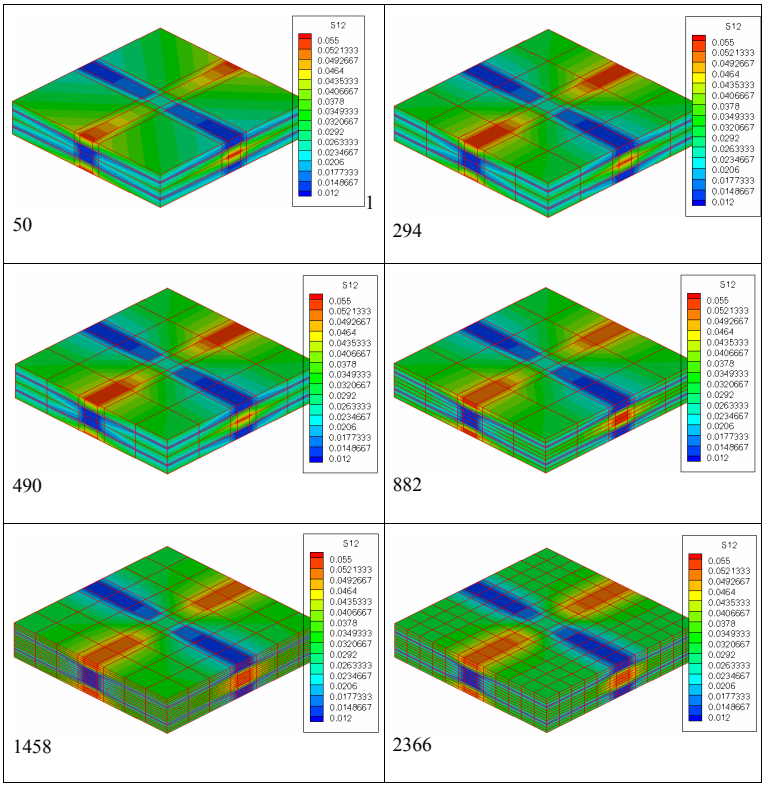

Figure 13: Effect of micromesh size on the computed local $\bar{\tau}_{12}$ distribution, applied overall strain $\bar{\gamma}_{12}$= 1.5%

An important observation to make here is the increase in the slope of the stress-strain curve seen under axial tensile straining (Fig. 15) following the transverse splitting of the fiber bundle aligned with the x_1-axis. Keeping in mind that apart from the increased $\bar{\varepsilon}_{11}$ strain applied to the woven composite, all other overall strain components are zero in this example. For the sake of simplifying the discussion, consider only the effect of the constraint $\bar{\varepsilon}_{22}$=0. A simple calculation of the normal stress generated in the direction of the x_1-axis provides $\bar{\sigma}_{11} = \bar{\varepsilon}_{11} E_1/(1-\nu_{12}\nu_{12})$. Since the effect of transverse damage is to increase Poisson ratios, it will lead to a higher effective modulus in the loading direction.

For in-plane shear straining, Fig. 16, the bulk matrix damage appears at the earliest but it has no effect on the overall stiffness. It is followed by the fiber bundle sliding modes parallel to the in-plane axes, which together with the transverse shear

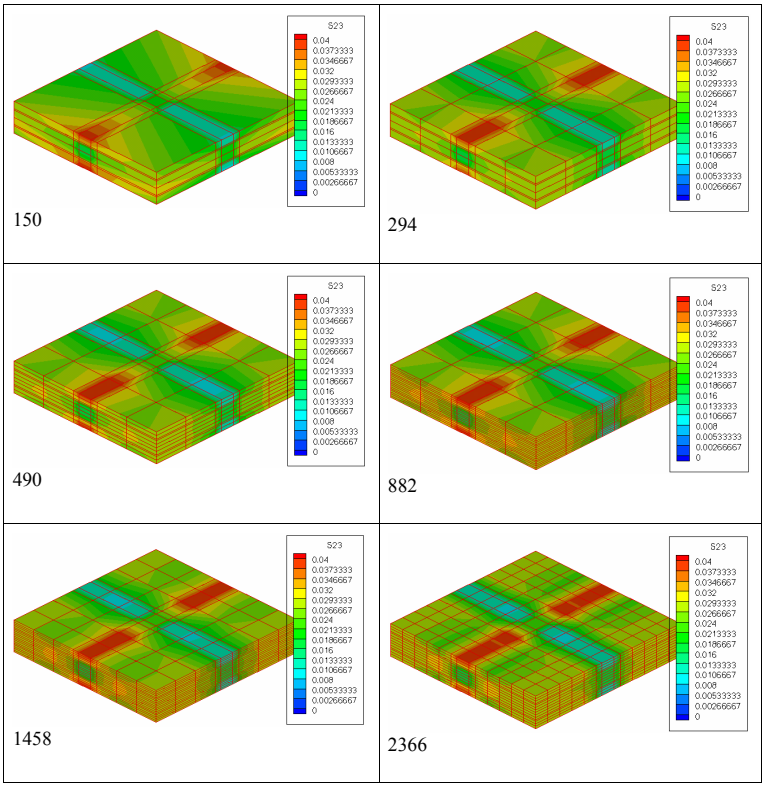

Figure 14: Effect of micromesh size on the computed local $\bar{\sigma}_{23}$ distribution, applied overall strain $\bar{\sigma}_{23}$= 0.8%

sliding of the fiber bundles cause significant drop in the overall stress. For transverse shear loading, Fig. 17, the bulk matrix damage and the fiber sliding damage modes appear earlier but the eventual stress loss is precipitated by sliding of the interfaces perpendicular to the z-fiber. For out-of-plane tensile loading, the only damage mode active is peeling of the interface layer and it brings down the stress precipitously.

The appearance and growth details of the individual damage modes are important in fine tuning the individual constituents of the composite. Although the direct strength properties are important, the sliding modes indicate the importance of increasing the transverse shear strength which may be achieved by modifying the resin characteristics.

In Figs. 15-17, the results from the 1458 sub-volume RVE micromesh are used for

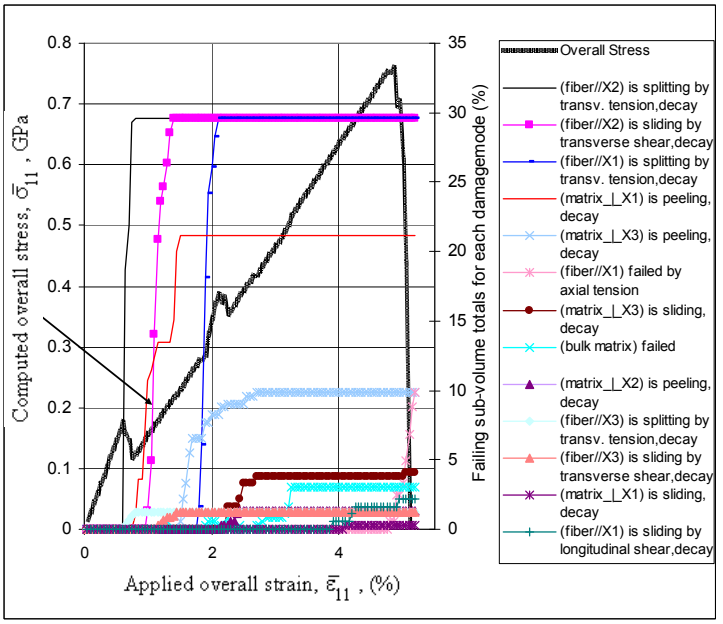

Figure 15: Effect of progressing damage modes on $\bar{\sigma}_{11}$ vs. $\bar{\varepsilon}_{11}$ response

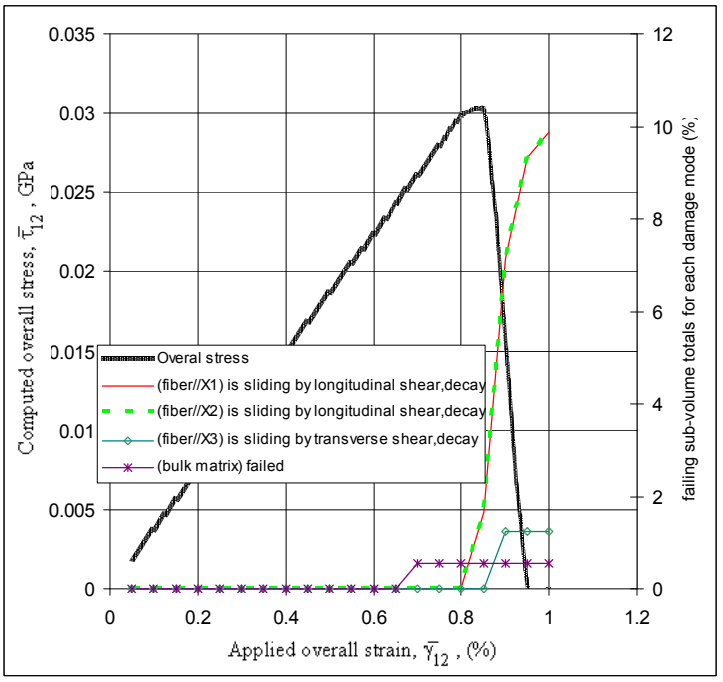

Figure 16: Effect of progressing damage modes on $\bar{\tau}_{12}$ vs.$\bar{\gamma}_{12}$ response

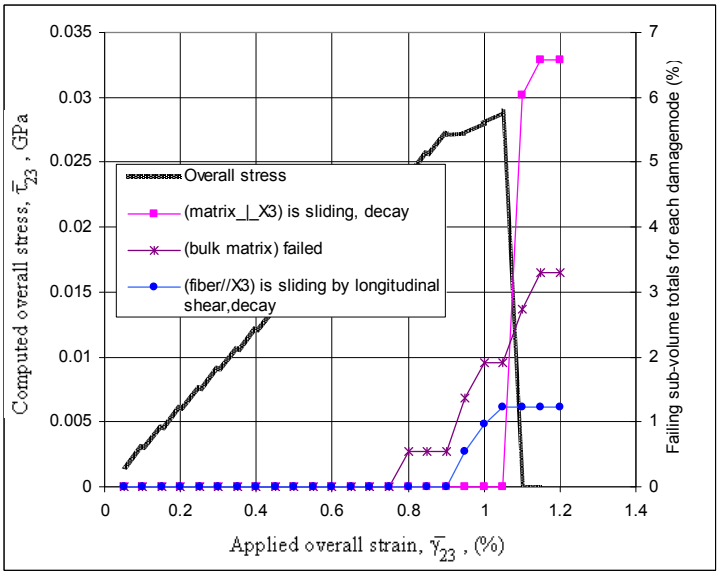

Figure 17: Effect of progressing damage modes on the $\bar{\tau}_{23}$ vs. $\bar{\gamma}_{23}$ response

the overall stress vs. strain curves, and for the sub-volume counts for the individual damage modes. Similar trends are also found for other RVE mesh sizes, and in Figs. 18-21, the totals of the counts of sub-volumes that are affected by all the damage modes are presented vs. the respective applied overall strains.

As can be seen in Fig. 18, all the RVE mesh sizes show the same growth trend for the totals of the damage affected sub-volumes with respect to the applied in-plane strain. The totals of the damage affected sub-volumes are presented with respect to the applied out-of-plane strain, in Fig. 19. The results for longitudinal shear loading and transverse shear loading are shown in Figs. 20-21, respectively. All these four cases are matrix dominated. The strain range in which the first damage mode appears and the eventual stress loss occurs is small $\sim 0.1\%$. Similarly the number of sub-volumes available for the spread of the damage, i.e. the number of interface sub-volumes, is also limited. This explains the variation found in the predictions by the different RVE meshes for these loading cases. Even then all the RVE meshes show identical damage modes and their onset at approximately the same applied strains.

RVE-TFA provides global stresses, the local stresses and local damage evolution in the microstructure. Based on the predicted overall stresses vs. the applied overall strains (Figs. 4-7) and the total strain energy densities, maximum overall stresses

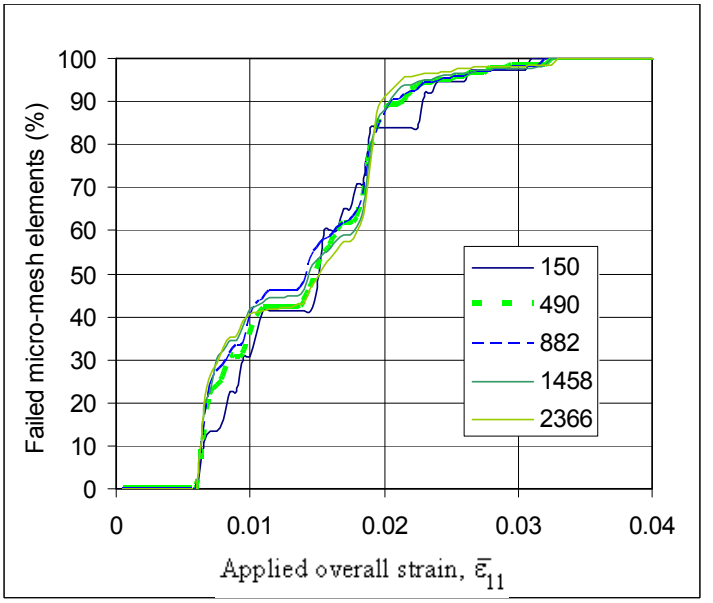

Figure 18: Mesh effect on the accumulation of damaged elements for all damage modes under the $\bar{\sigma}_{11}$ vs. $\bar{\varepsilon}_{11}$ loading

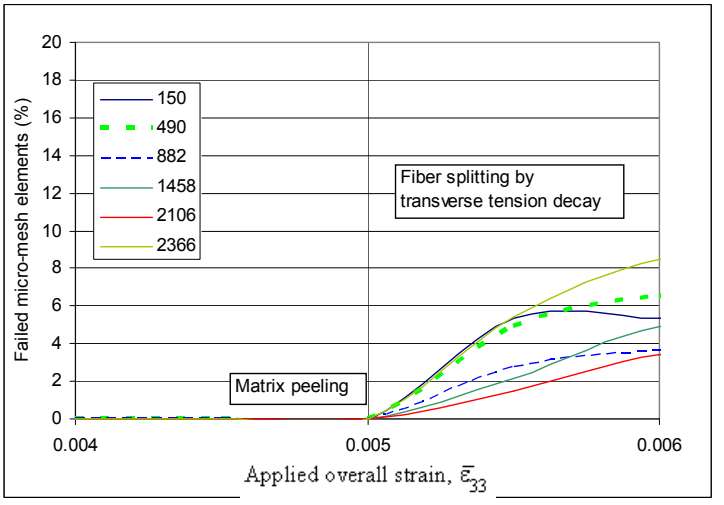

Figure 19: Mesh effect on the accumulation of damaged elements for all damage modes under the $\bar{\sigma}_{33}$ vs. $\bar{\varepsilon}_{33}$ loading

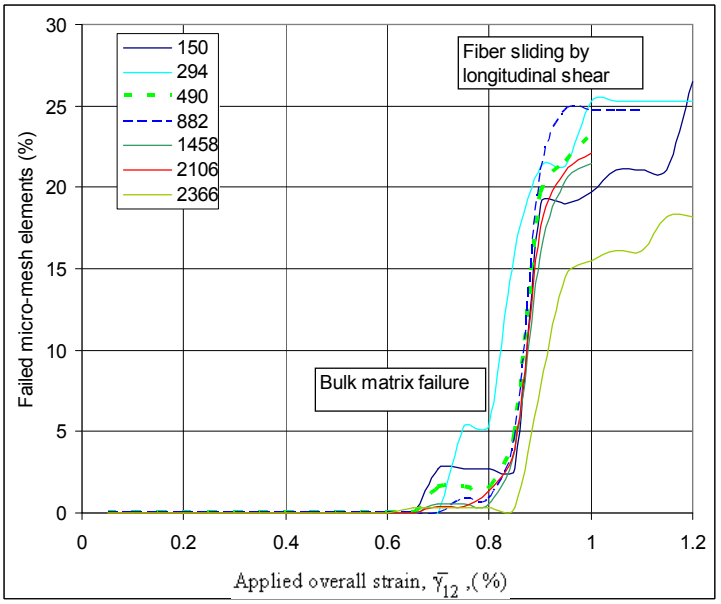

Figure 20: Mesh effect on the accumulation of damaged elements for all damage modes under the $\bar{\tau}_{12}$ vs. $\bar{\gamma}_{12}$ loading

and failure strains (Figs. 8-10), it may be concluded that an RVE-TFA can be implemented with approximately ∼490 sub-volumes for conducting dual level global-local impact analyses of 3-D woven composites. Based on the computed local RVE stress distributions (Figs. 11-14), and the demonstrated ability for predicting the dominant damage modes in each of the applied overall strain loadings (Figs. 15-17), and the accumulations of the subvolumes damaged by the dominant damage modes (Figs. 18-21), an RVE mesh size ∼490 can also be deemed to be sufficient to approximately describe both the stress picture and the spreading damage in the RVE at the composite weave level and thus can be suitable for conducting RVE based 3-D woven composite design studies.

5 Conclusions and Future Work

An RVE micro-structural model of a 3D woven composite is investigated for the requirement of the mesh size for capturing the weave details and the growth of local damage modes. The damage modes considered are typical of those observed in quasi-static and low-velocity impacts of woven composites. They included matrix cracking, frictional sliding and debonding of the fiber bundles, and fiber rupture.

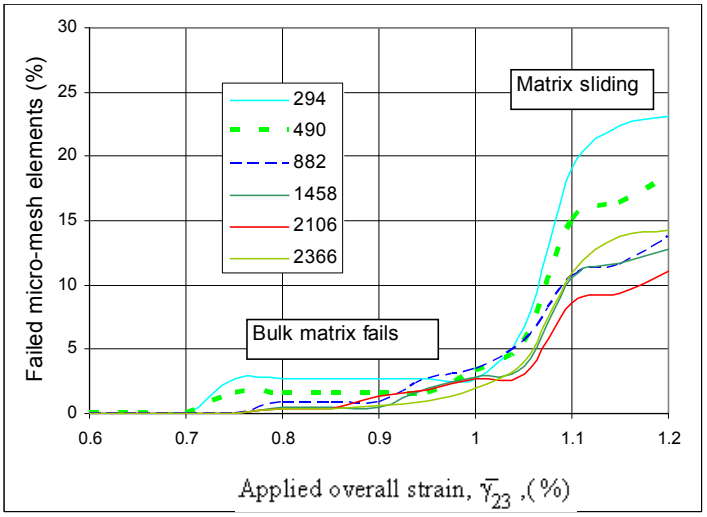

Figure 21: Mesh effect on the accumulation of damaged elements for all damage modes under the $\bar{\tau}_{23}$ vs. $\bar{\gamma}_{23}$ loading

The local stresses are obtained using a transformation field analysis (TFA) as sums of the elastic undamaged response and the contributions of auxiliary transformation stress fields for the selected damage modes.

A number of mesh sizes are considered for the RVE to capture the damage modes that spread locally at the weave level. The damage progression was considered indirectly by letting the progressing damage modes control the local stresses in the RVE sub-volumes and using accumulations of such sub-volumes as a measure of the spread of the local damage modes. The computed response included the local and overall stresses and the on-set and progression of the local damage modes. All the mesh sizes are shown to predict both the overall stresses and the accumulations of the locally damaged sub-volume totals under simple overall strain loading conditions.

The proposed micromechanics model and the TFA-based computational approach offer a robust method for evaluating the overall response of woven systems. The overall stress increments for an RVE and local damage modes' growth in it are computed by considering the accumulated stress and damage history only. Previous damage states, however, are not abolished but are recorded through local stress-to-strength ratios. However, to generalize the central conclusion of this study that a reasonable RVE mesh size $\sim$490 can be set needs further evaluation possibly for additional applied strain regimes, un-loading/re-loading paths, high velocity

impacts, and additional weave architectures as well as material systems.

Acknowledgement: The authors are grateful to Dr. Yehia Bahei-El-Din, who is currently with the British University, Cairo, Egypt, for his suggestions to the manuscript. This work was partially funded by the U.S. Army Research Office, Durham, NC. The simulations were performed in Army's MSRC at Aberdeen Proving Ground, MD.

References

Abu Al-Rub, R. K.; Voyiadjis, G. Z. (2006): A finite strain plastic-damage model for high velocity impact using combined viscosity and gradient localization limiters: Part I -Theoretical formulation, *International Journal of Damage Mechanics,* vol. 15, pp. 293-334.

Atluri, S.N. (2004): *The Meshless Method (MLPG) for Domain & BIE Discretizations*. ISBN:0-9657001-8-6, Tech Science Press.

Bahei-El-Din, Y. A. (1996): Finite Element Analysis of Viscoplastic Composite Materials and Structures. *Mechanics of Composite Materials and Structures*, vol. 3, pp. 1-28.

Bahei-El-Din, Y. A.; Botrous, A. G. (2003): Analysis of progressive fiber debonding in elastic laminates, *International Journal of Solids and Structures*, vol. 40, pp. 7035-7055.

Bahei-El-Din, Y. A.; Rajendran, A. M.; Zikry, M. A. (2004): A micromechanical model for damage progression in woven composite systems. *International Journal of Solids and Structures*, vol. 41, pp. 2307-2330.

Bahei-El-Din, Y. A.; Rajendran, A. M.; Valisetty, R.; Namburu, R. (2007): Scalable RVE-Preprocessor for TFA Analysis of 2D Glass Fiber Reinforced Plastics (GRP) Woven Composite Laminates for Use in the Transformation Field Analysis (TFA) Based Constitutive Model Algorithm in PARADYN3D Code. Final Report, Army Research Office Scientific Services Program, Contract No. DAAD19-02-D-0001, TCN 06188.

Bogdanovich, A. E.; Pastore, C. M. (1996): Material smart analysis of textile reinforced structures. *Compoites Science and Technology*, vol. 56, pp. 291-309.

Caiazzo, A. A.; Costanzo, F. (2001): Modeling layered composites with evolving cracks. *International Journal of Solids and Structures*, vol. 38, pp. 3469-3485.

Chou, S. C.; Deluca, E. (1993): *Dynamic Response of S-2 Glass Reinforced Plastic Structural Armor,* Technical Report, Army Research Laboratory, ARL-SR-5.

Dvorak, J. J.; Teply, J. L. (1985): Periodic Hexagonal Array Models for Plas-

ticity Analysis of Composite Materials. *Plasticity Today: Modeling, Methods and Applications*, Editors: Sawczuk, A. and Bianchi, V., W. Olaszak Memorial Volume, Elsevier Scientific Publishing Co., Amsterdam, pp. 623-642.

Dvorak, G. J. (1992): Transformation fields analysis of inelastic composite materials. *Proceedings of the Royal Society*, vol. A437, pp. 311-327.

Dvorak, G. J.; Bahei-El-Din, Y. A.; Wafa, A. M. (1994): Implementation of the transformational field analysis for inelastic composite materials. *Computational Mechanics*, vol. 14, pp. 201-208.

Dvorak, G. J.; Zhang, J. J. (2001): Transformation field analysis of damage evolution in composite materials. *Journal of Mechanics and Physics of Solids,* vol. 49, pp. 2517-2541.

Ghosh, S.; Lee, K.; Moorthy, S. (1995): Multiple scale analysis of heterogeneous elastic structures using homogenization theory and Voronoi cell finite element method. *International Journal of Solids and Structures*, vol. 32, pp. 27-62.

Han, Z. D.; Rajendran, A.M,; Atluri, S.N. (2005): Meshless Local **Petrov-Galerkin** (MLPG) Approaches for solving nonlinear problems with large deformationand rotation. *CMES: Computer Modeling in Engineering & Sciences*, vol. 10, no. 1, pp. 1-12.

Hill, R. (1963): Elastic properties of reinforced solids: some theoretical principles. *Journal of Mechanics and Physics of Solids,* vol. 11, pp. 357–372.

Hill, R. (1965): A self-consistent mechanics of composite materials. *Journal of Mechanics and Physics of Solids,* vol. 13, pp. 213–222.

Kim, J. K.; Sham, M. L. (2000): Impact and delamination failure of woven-fabric composites. *Composites Science and Technology*, vol. 60, pp. 745-761.

Liu, H.T.; Han, Z. D.; Rajendran, A. M.; Atluri, S.N. (2006): Computational Modeling of Impact Response with the RG Damage Model and the Meshless Local **Petrov-Galerkin** (MLPG) approaches. *CMC: Computers, Materials, & Continua*, vol. 4, pp. 43-53.

Oskay, C.; Fish, J. (2007): Eigendeformation-based reduced order homogenization for failure analysis of heterogeneous materials. *Computational Methods in Applied Mechanics and Engineering,* vol. 196, pp. 1216–1243.

Qiu, Y.; Xu, W.; Wang, Y.; Zikry, M. A. (2001): Fabrication and characterization of three-dimensional cellular matrix composites reinforced with woven carbon fabric. *Compoites Science and Technology*, vol. 61, pp. 2425–2435.

Shah Khan, M. Z.; Simpson, G. (2000): Mechanical properties of a glass reinforced plastic naval composite material under increasing compressive strain rates. *Materials Letters*, vol. 45, pp. 167–174.

Tsai, L.; Prakash, V.; Rajendran, A. M.; Dandekar, D. P. (2007): Structure of shock waves in glass fiber reinforced polymer matrix composites. *Applied Physics Letters,* vol. 90.

Valisetty, R.; Namburu, R.; Rajendran, A. M.; Bahei-El-Din, Y. A. (2004): Scalable coupling of TFA and PARADYN analyses for impact modeling of 3-d woven composites. Proceedings of the 2004 International Conference on Computational & Experimental Engineering & Sciences, Tech Science Press, pp. 92-97.

Voyiadjis, G. Z.; Kattan, P. I. (2009): A comparative study of damage variables in continuum damage mechanics, *International Journal of Damage Mechanics,* vol. 18, pp. 215-340.